Remote Sensing of Environment 209 (2018) 19–30

Contents lists available at ScienceDirect

Remote Sensing of Environment

journal homepage: www.elsevier.com/locate/rse

First hyperspectral imaging survey of the deep seafloor: High-resolution mapping of manganese nodules

Ines Dumke[a,*], Stein M. Nornes[a], Autun Purser[b], Yann Marcon[b,c], Martin Ludvigsen[a], Steinar L. Ellefmo[d], Geir Johnsen[e], Fredrik Søreide[a]

[a] Department of Marine Technology, Norwegian University of Science and Technology (NTNU), Otto Nielsens vei 10, 7491 Trondheim, Norway
[b] Alfred Wegener Institute, Helmholtz Centre for Polar and Marine Research, Am Handelshafen 12, 27570 Bremerhaven, Germany
[c] MARUM, Center for Marine Environmental Sciences, Leobener Str. 2, 28359 Bremen, Germany
[d] Department of Geoscience and Petroleum, Norwegian University of Science and Technology (NTNU), Sem Sælands vei 1, 7491 Trondheim, Norway
[e] Centre for Autonomous Marine Operations and Systems, Department of Biology, Norwegian University of Science and Technology (NTNU), 7491 Trondheim, Norway

ARTICLE INFO

Keywords:
Hyperspectral imaging
Underwater Hyperspectral Imager (UHI)
Manganese nodules
DISCOL
Supervised classification
Support Vector Machine
Spectral Angle Mapper

ABSTRACT

Hyperspectral seafloor surveys using airborne or spaceborne sensors are generally limited to shallow coastal areas, due to the requirement for target illumination by sunlight. Deeper marine environments devoid of sunlight cannot be imaged by conventional hyperspectral imagers. Instead, a close-range, sunlight-independent hyperspectral survey approach is required. In this study, we present the first hyperspectral image data from the deep seafloor. The data were acquired in approximately 4200 m water depth using a new Underwater Hyperspectral Imager (UHI) mounted on a remotely operated vehicle (ROV). UHI data were recorded for 112 spectral bands between 378 nm and 805 nm, with a high spectral (4 nm) and spatial resolution (1 mm per image pixel). The study area was located in a manganese nodule field in the Peru Basin (SE Pacific), close to the DISCOL (DISturbance and reCOLonization) experimental area. To test whether underwater hyperspectral imaging can be used for detection and mapping of mineral deposits in potential deep-sea mining areas, we compared two supervised classification methods, the Support Vector Machine (SVM) and the Spectral Angle Mapper (SAM). The results show that SVM is superior to SAM and is able to accurately detect nodule surfaces. The UHI therefore represents a promising tool for high-resolution seafloor exploration and characterisation prior to resource exploitation.

1. Introduction

Hyperspectral imaging is defined as the acquisition of images in hundreds of contiguous spectral bands so that a full spectrum is recorded for each image pixel (Goetz et al., 1985; Goetz, 2009). Each pixel spectrum contains different spectral components arising not only from the surface material or vegetation, but also from water, atmosphere, the illumination source (typically the sun), and the hyperspectral sensor itself.

Calibrations are required to correct for any external influences and obtain a reflectance spectrum specific for the objects of interest (OOI) and representing the percentage of light reflected by the OOI for each wavelength. Different OOI differ in their reflectance spectra, providing so-called “optical fingerprints”. By comparing each pixel's reflectance spectrum to reference spectra obtained from, e.g. a spectral library or field samples, reflectance spectra can be used to classify OOI and produce coverage maps based on spectral signatures.

Hyperspectral data are typically acquired by passive hyperspectral imagers that use the sun as light source and record reflected solar radiation (and other spectral components associated with external influences) over a wavelength range of 400–2500 nm (e.g. Resmini et al., 1997; Kruse et al., 2003; Dickey et al., 2006), thus covering the visible range (400–700 nm) and part of the infrared portions (> 700 nm) of the solar spectrum. Most passive imagers are either airborne or spaceborne. In addition, passive hyperspectral imagers or spectroradiometers for underwater use have been developed over the past two decades to measure in-situ optical properties of the ocean, e.g. operated at mooring stations or by divers (Mazel, 1997; Hochberg and Atkinson, 2000; Pons et al., 2007; Ramírez-Pérez et al., 2015).

Hyperspectral imaging has been used mostly in terrestrial settings, but has also been applied in the marine environment. Terrestrial applications include mapping of vegetation (Underwood et al., 2003; Adam et al., 2010; Landmann et al., 2015), infrastructure (Roessner et al., 2001; Dell'Acqua et al., 2004; Herold et al., 2004), and surface

* Corresponding author at: GEOMAR Helmholtz Centre for Ocean Research Kiel, Wischhofstr. 1-3, 24148 Kiel, Germany.
E-mail address: idumke@geomar.de (I. Dumke).

https://doi.org/10.1016/j.rse.2018.02.024
Received 17 June 2017; Received in revised form 21 December 2017; Accepted 16 February 2018

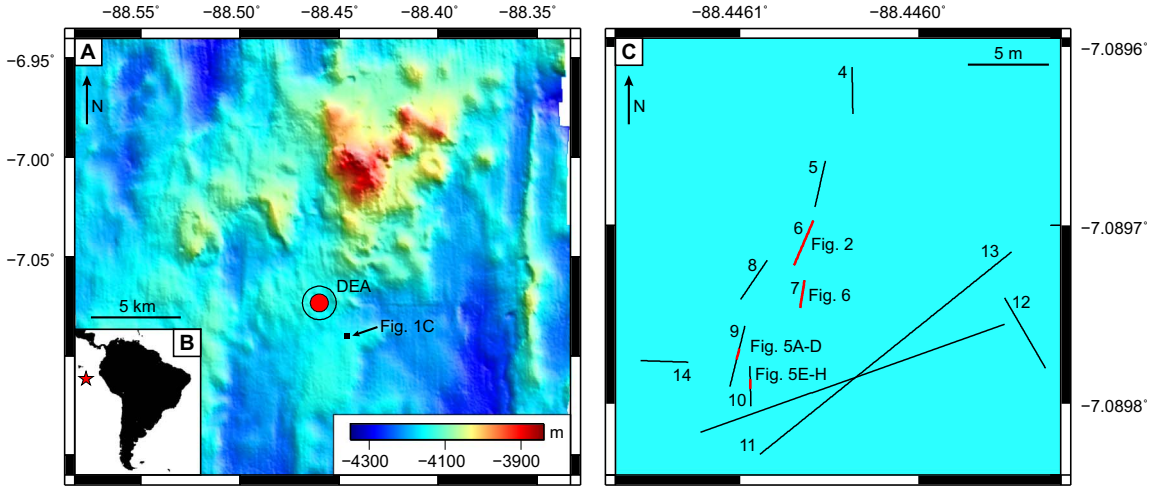

Fig. 1. (a) Bathymetric map (50 m resolution, courtesy of GEOMAR) showing the location of the study area in (c) and the DISCOL experimental area (DEA) in the Peru Basin. The filled red circle represents the central DISCOL area (1 km radius), the black circle marks the outer extent of the disturbance experiment (1.877 km radius). (b) Overview map indicating the location of the DEA offshore Peru (red star). (c) Locations of the main 11 survey tracks (tracks 4–14) to which supervised classification was applied. Bathymetry colour scale is the same as in (a); the water depth in the study area is about 4195 m. (For interpretation of the references to colour in this figure legend, the reader is referred to the web version of this article.)

minerals (e.g. Resmini et al., 1997; Bierwirth et al., 1999; Sabins, 1999; Kruse et al., 2003). The main motivation for hyperspectral mapping of mineral distribution is the detection of ore deposits for mineral exploration purposes (Bierwirth et al., 1999; Sabins, 1999; van der Meer et al., 2012). In marine settings, hyperspectral methods have been used mainly in oceanographic and biological studies (Chang et al., 2004; Dickey et al., 2006), including mapping of ocean colour (Dickey et al., 2006; Dierssen and Randolph, 2013) and seafloor habitats (Klonowski et al., 2007; Fearns et al., 2011) such as reefs (Hochberg and Atkinson, 2000, 2003; Kutser et al., 2006; Petit et al., 2017), seagrass ecosystems (Dierssen, 2013; Dierssen et al., 2015), and kelp forests (Volent et al., 2007). Given that the majority of sunlight penetrates no deeper than 50 m into water, the application of passive hyperspectral sensors in marine settings is limited to coastal areas and shallow water depths (e.g. Klonowski et al., 2007; Volent et al., 2007; Fearns et al., 2011).

More recently, active hyperspectral imagers for underwater applications have been developed (Chennu et al., 2013; Johnsen et al., 2013; Tegdan et al., 2015). Active hyperspectral sensors use their own external light sources for target illumination, thus allowing seafloor studies in water depths with no natural light penetration. Due to the strong in-water attenuation of wavelengths in the near-infrared and infrared part of the spectrum, these underwater hyperspectral sensors are limited to the visible range of wavelengths.

The first active underwater hyperspectral imagers were mounted on mechanical sledges or carts operated on the seafloor in shallow water depths (< 6 m), with illumination provided by two halogen lamps (Chennu et al., 2013; Johnsen et al., 2013; Pettersen et al., 2014). Since then, scientific Underwater Hyperspectral Imagers (UHIs) developed by Ecotone AS (Trondheim, Norway) have been deployed on remotely operated vehicles (ROVs) in water depths of up to 600 m. The UHIs have a spectral range of 378–805 nm, with a spectral resolution of up to 0.5 nm (Johnsen et al., 2013, 2016; Tegdan et al., 2015), and have been used to study e.g. cold-water corals and kelp forests in the Trondheimsfjord (Tegdan et al., 2015; Johnsen et al., 2016), a vertical rock wall at Haugbergneset (Tegdan et al., 2015), benthic organisms in Kongsfjorden, Svalbard (Johnsen et al., 2016), and a wreck site at Trygghamna, Svalbard (Daase, 2016). In addition to ROVs, autonomous underwater vehicles (AUVs) can also serve as UHI mounting platforms (Johnsen et al., 2013). A first AUV-based UHI survey was recently conducted successfully at the Arctic Mid-Ocean Ridge as part of the MarMine project (Ludvigsen et al., 2016; Sture et al., 2017).

The majority of these underwater hyperspectral studies focused on biological OOIs, but Johnsen et al. (2013) demonstrated that UHIs can also be used for mapping of seafloor minerals. As with terrestrial mineral deposits, seafloor mineral deposits may be detected and characterized based on their spectral signatures. Provided a sufficient sensor depth-rating, underwater hyperspectral imaging may therefore be of interest for exploration in potential deep-sea mining areas. Although not yet an active industry, deep-sea mining is predicted to start within the next decade in areas of prospective seafloor mineral deposits such as manganese nodules and massive sulphide deposits (Glasby, 2002; Rona, 2003; Gwyther, 2008; Hoagland et al., 2010). A detailed seafloor mapping and characterisation of mineral deposits, as well as fauna distribution and understanding of ecosystem functioning in these remote seafloor areas is required prior to exploitation.

Manganese nodules are seafloor mineral deposits that grow concentrically around a nucleus, usually at the sediment-water interface. In addition to Mn and Fe, the nodules typically contain Ni, Cu, Co, and Zn, which are supplied either by the underlying sediments (diagenetic deposits) or by seawater (hydrogenous deposits) (e.g. Glasby, 2000). Nodule compositions can vary on regional as well as local scales (e.g. Cronan and Tooms, 1969; Glasby, 1972, 2000), and it is this mixed composition which has rendered manganese nodules an important potential resource for exploitation. Dimensions are generally between < 3 cm and > 10 cm, and growth rates are hypothesised to be 2–100 mm Myr^{-1} (e.g. Glasby, 2000). Manganese nodules are found in deep-sea basins (> 4000 m water depth) characterized by low sedimentation rates (< 5 mm kyr^{-1}), with major nodule regions including the Clarion-Clipperton Zone in the equatorial North Pacific, the Central Pacific Basin, and the Peru Basin.

Here, we present the first hyperspectral image data of the seafloor in water depths > 600 m. The data were acquired by a new deep-sea UHI in a manganese nodule field in the Peru Basin (SE Pacific) in 4195 m water depth. We compare two supervised classification methods and estimate nodule coverage for the surveyed area from the classification results. We also evaluate the potential of underwater hyperspectral imaging as an exploration method in prospective deep-sea mining areas.

2. Study area

The study area was located in a manganese nodule field in the Peru Basin (SE Pacific Ocean) in about 4195 m water depth (Fig. 1a). It was situated about 700 m southeast of the DISCOL (DISturbance and reCOLonization) experimental area (DEA), which comprises a generally flat, circular area of 10.8 km^2 in 4140–4200 m water depth (Thiel and

Schriever, 1989; Foell et al., 1990; Borowski, 2001). Surface sediments consist of 7–10 cm of dark brown silicate oozes overlaying lighter-coloured clays enriched in biogenic carbonate (Borowski, 2001). Manganese nodules in the area have diameters of up to 15 cm, with a nodule density estimated to be 5–10 kg m^{-2}, prior to the DISCOL experiment (Thiel and Schriever, 1989).

The DISCOL experiment was conducted in 1989 in order to simulate potential effects of deep-sea mining equipment and monitor the impact of these on benthic communities (Thiel and Schriever, 1989; Foell et al., 1990). Within the DEA, the seafloor was disturbed by a "plough-harrow" device towed along 78 straight tracks that crossed the centre of the DEA (Thiel and Schriever, 1989; Foell et al., 1990; Borowski and Thiel, 1998). Besides the direct disturbance of the seabed, the experimental plough harrow buried the manganese nodules within the ploughtracks into the sediments, and produced a sediment plume that later settled out across both ploughed and unploughed areas (Foell et al., 1990; Schriever, 1995).

Since 1989, the DEA has been revisited several times to monitor the recolonization process via video surveys and physical sampling. After a strong reduction in abundance of all faunal taxa immediately after the experiment, recolonization started rapidly but had not reached pre-impact conditions even seven years after the experiment (Schriever, 1995; Borowski and Thiel, 1998; Borowski, 2001). In 2015, 26 years after the experiment, the area was revisited by the RV SONNE cruises SO242/1 and SO242/2. Detailed mapping and sampling campaigns, including ROV and AUV surveys, revealed that the disturbance tracks were still visible after 26 years, manganese nodules within and near the DEA were either partly covered by sediment or completely buried, and from preliminary results currently being analysed, faunal communities remain distinct from those present within the DEA prior to the disturbance (Greinert, 2015; Boetius, 2015).

3. Methods

3.1. Data acquisition

Hyperspectral data were acquired in 2015 during the RV SONNE cruise SO242/2 with a new UHI (UHI #4) developed by Ecotone AS (Trondheim, Norway). The UHI is depth-rated to 6000 m and was tested in this study for the first time. It is a push-broom scanner with beam-widths of 60° (transverse) and 0.4° (longitudinal) and is mounted looking vertically downwards to record lines of 1600 pixels perpendicular to the track direction. Intensities of reflected light can be measured for up to 896 spectral bands between 378 and 805 nm, with recording frequencies of up to 100 Hz. In this study, data were recorded at 20 Hz with spectral binning of 8, resulting in 112 spectral bands with a spectral resolution of 4 nm.

The KIEL6000 ROV (GEOMAR) was used as the sensor platform for the UHI. For data acquisition, the UHI was mounted on the fully outstretched manipulator arm of the ROV. With this setup, it was not possible to accommodate UHI-dedicated light sources on either side of the sensor, as is normally preferred (Johnsen et al., 2013, 2016; Tegdan et al., 2015). Seafloor illumination was instead provided by the ten ROV light sources, which included an LED, seven halogen lamps (five Deep Multi-SeaLite lamps and two Sea Arc 5000 lamps), and two HMI lamps (SeaArc2). This illumination from behind and above the UHI was not optimal, and resulted in two kinds of shadows in the recorded data: a constant dark shading across half of the swath, due to the manipulator arm blocking part of the light, and shadows on nodule sides facing away from the ROV, caused by the illumination source positioned behind the UHI.

A total of 15 tracks with constant speed (0.05 m s^{-1}) and heading were acquired within a 20 × 40 m^2 area containing manganese nodules and different benthic fauna (ROV dive SO242/2_191-1; Boetius, 2015). Track length ranged between 1.7 m and 4.9 m except for two tracks with lengths of 20 m (Fig. 1c). ROV altitude was approximately 1–1.2 m, resulting in a track width of 1–1.2 m and an across-track resolution of about 1 mm per pixel.

ROV navigation was provided by POSIDONIA ultra-short baseline (USBL) positioning with an accuracy of about 0.02% of the water depth. Position data were recorded at < 0.25 Hz and ROV attitude data (velocity and orientation) were logged at 1 Hz. In addition to the UHI data, SD and HD video data were acquired on all tracks. The video data were used to identify larger seabed fauna (Dumke et al., in prep.), and frame grabs from the HD and SD video data served as a basis for upsampling of the navigation data (see Section 3.2.3 and Nornes et al. (in prep.)).

3.2. Data processing

Processing of the hyperspectral images consisted of three steps: (1) calibration of the raw data (digital counts) to radiance data (in W m^{-2} sr^{-1} nm^{-1}) by correcting for sensor-specific influences, (2) conversion of radiance to reflectance by correcting for external influences from illumination sources and the inherent optical properties of the water column, and (3) geocorrection. The desired output is reflectance data that only depends on the seafloor material and OOI.

3.2.1. Radiance processing

Calibration of raw data to radiance data was done through radiometric correction using the Hypermap software tool (Ecotone). The radiance data were then loaded into MATLAB (MathWorks Inc.) and formatted as a 3-dimensional array $A(m,n,i)$ of m lines (number of lines along the track), n samples (number of pixels of the UHI slit, or across the track), and i spectral bands. As the outer bands (< 400 nm and > 710 nm) were rather noisy, spectral subsetting was done to reduce the data to the 83 bands between 400 nm and 710 nm. In addition, spatial subsetting was performed to remove redundant lines at the track ends caused by the time lag between the end of the ROV track and the end of UHI data recording.

3.2.2. (Pseudo-) reflectance processing

Following radiance processing, the next step was the correction for external influences on the spectral characteristics of the reflected light. The main external influence was the illumination, which was relatively consistent along the track but varied laterally due to the setup-induced shadow. As the combined spectral characteristics of the ten ROV lamps could not be determined, the illumination influence was approximated by a reference spectrum calculated from the data collected during each track. For each sample n along the UHI slit, a reference spectrum $s_{ref}(n)$ was calculated as the median spectrum of all radiance spectra $s_{rad}(m,n)$ recorded for sample n over all lines m along a particular survey track. For each image pixel (m,n), the radiance spectrum was then divided by its respective reference spectrum:

$$s_{corr}(m,n) = \frac{s_{rad}(m,n)}{s_{ref}(n)} \quad (1)$$

where $s_{corr}(m,n)$ is the corrected spectrum for the image pixel (m,n). The spectra were then smoothed by a moving average filter with a window of 11 bands.

While this method worked well in general and removed effects that were constant in along-track direction, it did not take into account altitude variations, which change the light field occasionally along the track. However, most tracks were run at a relatively constant altitude of 1 m, and altitude effects were therefore considered to be negligible.

Correction by median spectra also takes into account the inherent optical properties of the water column, which were unknown for the area but were assumed to be constant during the period of study. Based on the high water depth and the video data, which showed that the sediment remained undisturbed during the survey period, we assumed optically clear waters with a likely negligible influence on the recorded spectral intensities.

3.2.3. Geocorrection via photomosaic-based navigation data

Due to the small scale of the imaged areas, some of which covered only 2 m^2, georeferencing of the UHI data required very high-resolution navigation data. The ROV's POSIDONIA USBL navigation had an accuracy of approximately 0.02% of the water depth, which thus amounted to ± 10 m in the study area. As the ROV navigation data contained frequent jumps of several metres and the recording frequencies (1 Hz for ROV velocity and orientation, < 0.25 Hz for position data) were generally too low for combination with the 20 Hz UHI data, the ROV navigation data did not provide satisfactory geocorrection of the UHI data.

In order to acquire navigation data of sufficient quality, the velocity and orientation data of the ROV were integrated to create a smooth relative position trajectory for each track, a process known as Dead Reckoning (DR; Fossen, 2011). The average USBL position recorded during the track was used to globally position the DR-derived track line. Using the photogrammetry and photomosaic software Agisoft PhotoScan, the DR-derived navigation was then combined with frame grabs from the HD and SD videos to produce upsampled and refined 5 Hz navigation data. This procedure is further detailed in Nornes et al. (in prep.).

The photomosaic-based navigation was corrected for a time shift between the navigation and the UHI data. Time shifts varied between 0 s (no shift) and −0.9 s. As the navigation data contained a few outliers, probably arising from noise introduced during image processing in Agisoft PhotoScan, a moving average filter with a window of 5 data points was applied to smooth the navigation data. Georeferencing, including correction for vehicle attitude influences, was done using the Hypermap software and the corrected data were output with a pixel size of 1 mm.

The correction by median spectra and subsequent geocorrection were able to remove most of the undesired external influences, including the setup-induced dark shading across the track. However, some residual influences, mostly from illumination, likely remain. The corrected data are therefore not true reflectance data, and are referred to as pseudo-reflectance data in the following.

3.3. Spectral classification

Based on the processing results, 11 of the tracks (Fig. 1c) were selected for spectral classification and further analyses. Classification was done using the ENVI software (v. 5.3; Exelis VIS) and two supervised classification methods, the Support Vector Machine (SVM) and the Spectral Angle Mapper (SAM), were applied. Both methods required training data as input for the classification. In the absence of an existing spectral library applicable to our study setting, training data were derived from the UHI data through user-defined regions of interest (ROIs). ROIs were defined manually for each track based on visual identification in the UHI “pseudo”-RGB data, which was composed of the three bands 645 nm (R), 571 nm (G), and 473 nm (B). In addition, visual comparisons of pixel spectra as well as the ROV video data were used to define ROIs.

The output of the spectral classification is a classification image showing the distribution of the different spectral classes on a pixel basis. In the following, we use the term “category” rather than “class” in order to differentiate it from the taxonomic rank “class” used in biological classification of organisms.

3.3.1. Support Vector Machine (SVM)

SVM is widely used in supervised classification and is based on statistical learning theory. Categories are separated by decision surfaces (hyperplanes) maximizing the margin between categories, with support vectors from the training data defining the points closest to the hyperplanes (Camps-Valls et al., 2004; Melgani and Bruzzone, 2004; Mountrakis et al., 2011, and references therein). SVM is often superior to other supervised classification methods (Melgani and Bruzzone, 2004; Bioucas-Dias et al., 2013) and also works well for noisy and complex data (Camps-Valls et al., 2004).

SVM classification was applied to the 11 tracks shown in Fig. 1c. The SVM results were compared to the UHI pseudo-RGB images for accuracy, as an alternative ground-truthing image did not exist. If necessary, SVM was rerun with improved ROIs. The SVM result was then smoothed using ENVI's classification aggregation tool to integrate smaller pixel clusters into the surrounding category. A pixel cluster threshold of 25–35 pixels was found to give the best balance between removing potential noise and loss of information.

3.3.2. Spectral Angle Mapper (SAM)

SAM is also a standard supervised classification method and is simpler and faster than SVM. Pixel spectra and endmember spectra from training data are treated as vectors in n-D space, where n corresponds to the number of spectral bands. Spectral similarity between a pixel spectrum and an endmember spectrum is determined from the angle between the two spectra and categories are assigned based on a defined maximum angle threshold (Kruse et al., 1993; Sohn and Rebello, 2002).

SAM was applied to only four tracks, as visual comparisons distinctly showed that the results were inferior to those of SVM. The same ROIs as for SVM were used. Initially, the maximum angle was set to the default value of 0.1 rad for all categories, but angles were adjusted after the first SAM run in order to improve the classification result. The default angle of 0.1 rad worked well for the background sediment. For the other categories, angles were either increased to up to 0.15 rad to increase classification sensitivity (e.g. for nodules, shadows, and most of the fauna), or decreased to 0.05 rad to reduce sensitivity and the number of false positives. The SAM results were smoothed via classification aggregation with a pixel cluster threshold of 25–30 pixels.

3.3.3. Relative classification accuracy

To determine the accuracy of a classification result, the classification image is normally compared to a ground-truthing image. However, no ground-truthing information, aside from the video data, was available. Therefore, this approach was used to compare the SAM results against the SVM results to determine the classification accuracy of SAM relative to SVM. The comparison was performed using ENVI's confusion matrix tool, which conducts a pixel-by-pixel comparison of a classification image (here: the SAM result) against a ground-truthing image (here: the SVM result). For each pixel in the SVM image, the location and category were compared to the corresponding location and category in the SAM image. The confusion matrix then output an overall accuracy, i.e., the number of pixels classified in the same way by both methods divided by the total number of pixels, as well as percentages of correctly classified pixels for each category.

3.4. Estimation of areal nodule density

The areal nodule density, or number of nodules per m^2, was determined from the amount of nodules identified in the UHI pseudo-RGB images of the nine shorter tracks (up to 5 m length) and verified by the video data. Manual nodule counting was not done for the two 20 m long tracks due to their length and associated high number of nodules, and because nodule distribution appeared to be similar to that of the shorter tracks.

In addition, we also tested if the areal nodule density can be estimated from quantitative analysis of the SVM classification images through automatic counting of nodule category areas. However, as shown below, the nodules appeared as very fragmented patches in the classification image, rather than one connected area per nodule. Automatic counting of nodule objects in the SVM image would consequently interpret each fragment as a separate nodule object and thus strongly overestimate the areal nodule density.

To obtain a better estimation, therefore, the classification image was

first smoothed by a classification aggregation of 300 pixels to remove the influence from very small pixel clusters. We then used ENVI's clump tool to grow and merge category areas belonging to the same nodule, as indicated by the UHI pseudo-RGB data. The clump tool clumps adjacent areas of the same category together by applying a dilate operation followed by an erode operation, both of which are controlled by a kernel of a user-defined size. Kernel sizes were 17–38 pixels for the dilate operation and 3–9 pixels for the erode operation. The clumping process was done in two ways. In case 1, clumping was applied only to the nodule category, while all other categories were merged into one background category. In case 2, clumping was done for both the nodule and the shadow category. The reason for case 2 was that some nodules were more conspicuous by their shadow than by nodule category pixels.

The resulting clump images were loaded into MATLAB and nodule objects were counted using a method by Reddy (2010) based on a foreground-background separation. The areal nodule density, which was calculated from the count results and imaged areas, was then compared to the reference density determined from the UHI pseudo-RGB images and video data.

4. Results

4.1. Quality of pseudo-reflectance data

The UHI pseudo-reflectance data are of generally good quality. For all tracks, the division by along-track median spectra completely removed the dark shading (Fig. 2a) caused by the influence of the ROV's manipulator arm on illumination, as shown by the example in Fig. 2b. Both manganese nodules and larger megafauna, e.g. the stalked sponge in Fig. 2b, are easy to distinguish from the relatively uniform background sediment. The data also show that most nodule surfaces are not fully exposed, but are partly or almost completely covered by sediment.

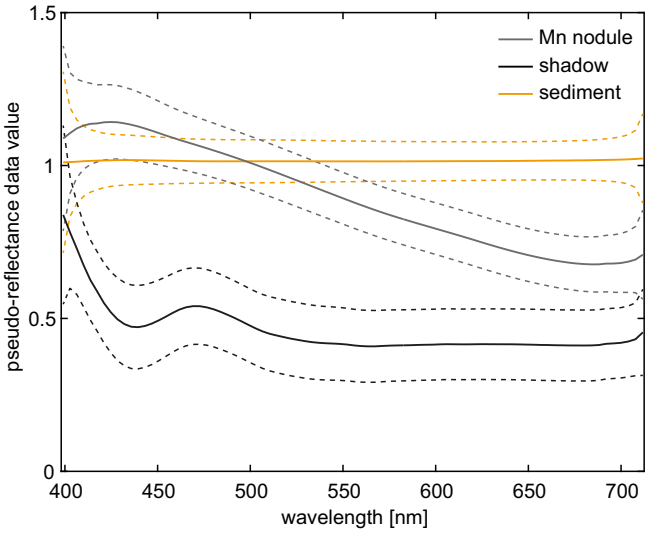

Fig. 3. Spectral responses for the three categories common to all tracks: manganese nodule, shadow (mostly behind nodules), and background sediment. Solid lines represent the mean spectrum based on ROIs of tracks 4–14, dashed lines mark the standard deviation.

Most nodules exhibit prominent shadows on the side facing away from the ROV lamps (Fig. 2a, b).

4.2. Supervised classification results

The same ROIs were used for the SVM and SAM classifications. In total, 20 categories were defined, three of which were common to all

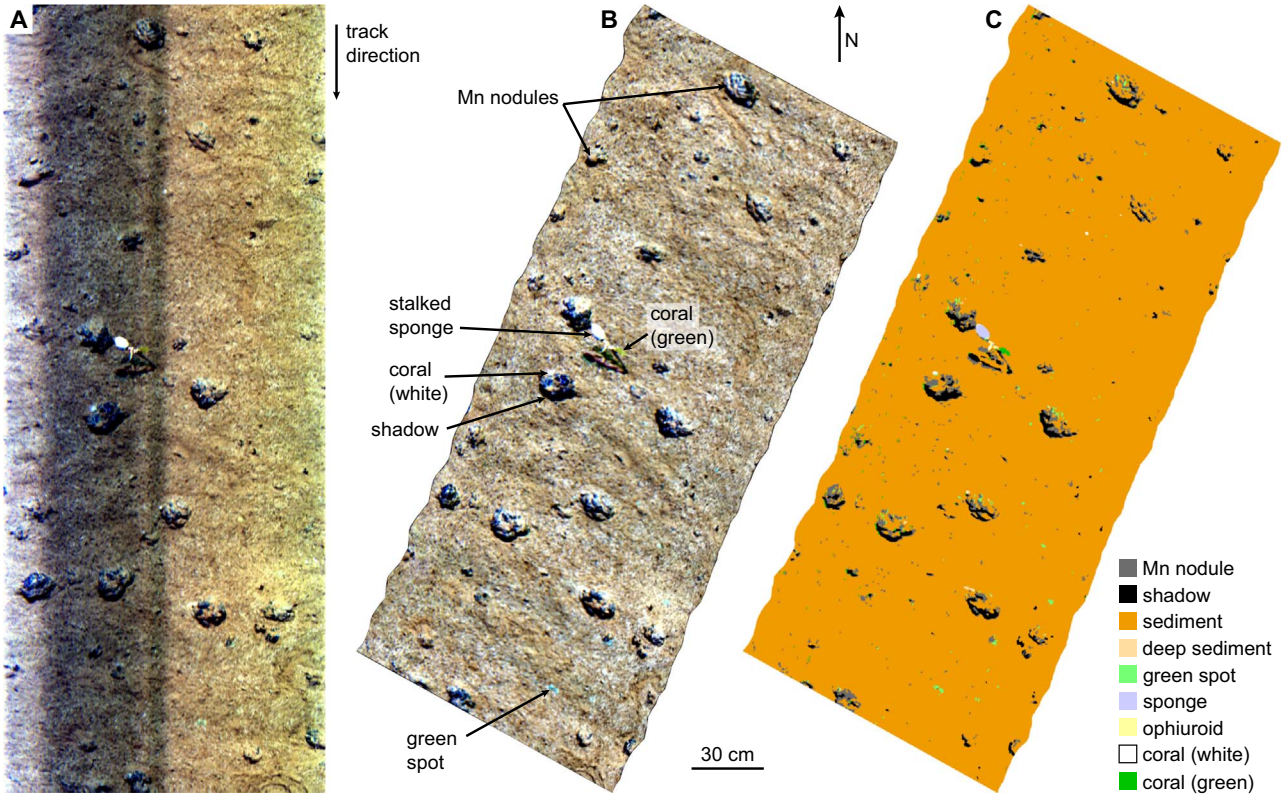

Fig. 2. (a) UHI radiance data in pseudo-RGB (R: 645 nm, G: 571 nm, B: 473 nm), showing manganese nodules and a stalked sponge (Hexactinellida) with an ophiuroid (brittle star, *Echinodermata ophiuroidea*) wrapped around the stalk. Note the dark shading caused by the ROV's manipulator arm blocking the light. (b) Geocorrected pseudo-reflectance data in pseudo-RGB. Division of each pixel spectrum by its corresponding along-track median spectrum completely removed the dark shadow. (c) SVM classification image based on the data in (b) and user-defined ROIs. Track location is shown in Fig. 1c.

tracks: nodule, sediment, and shadow. Mean spectra for these three categories are shown in Fig. 3. Although the shadows represented an illumination effect rather than seafloor material or fauna, it was necessary to include them as ROIs to avoid misclassification of the shadow areas. The sediment category represented the background sediment, i.e., the brown silicate oozes that typically constituted the surface sediment (Borowski, 2001). In addition, brighter sediment patches associated with light-coloured clays exposed from beneath the surface layer (Borowski, 2001) occurred on some tracks and were assigned to a separate category termed “deeper sediment”.

Based on taxa identification in the video data and the spectral characteristics, 16 spectral categories were defined for the megafauna, including sponges, corals, crustaceans, ophiuroids and dead salps. Further information is given in Dumke et al. (in prep.). Not all of these categories were present on each track; the number of fauna categories per track varied between one and six, with an average of 3.5.

In addition, one category was defined for distinct green spots in the UHI image. The associated spectra showed a minimum around 675 nm (Dumke et al., in prep.), which is characteristic for in vivo absorption of chlorophyll-a (e.g. Hakvoort et al., 1997). These spots may potentially represent increased concentrations of chlorophyll-a or degraded products associated with biomass that sank down to the seafloor from shallow waters (Dumke et al., in prep.).

4.2.1. SVM results

Comparison with the UHI pseudo-RGB images showed that the SVM classification results were relatively accurate. The exposed nodule surfaces were generally well classified, as were the larger types of megafauna (Figs. 2c, 4b, f). The nodules were commonly characterized by a combination of the nodule category and the shadow category, but they did not appear as connected nodule-shadow objects. Instead, they consisted of several small patches that belong to the nodule or shadow category and are surrounded by the background sediment category (Figs. 2c, 4b, f). In between the larger nodules, many small nodule and also shadow category patches were apparent even after classification aggregation of 25–35 pixels.

With a coverage of 94.7–97.5%, the background sediment category was by far the most dominant material category in the study area. Only 0.9–3.4% of the imaged surface areas were associated with nodules, while shadow areas constituted 1.0–2.6% (Fig. 5a). Combining the 16 fauna categories detailed in Dumke et al. (in prep.) resulted in a fauna coverage of < 0.5% of the seafloor. Both the green spots and deeper exposed sediment category had a maximum coverage of about 0.2% (Fig. 5a), with the deeper, light coloured sediment exposed on only five of the 11 tracks.

4.2.2. SAM results

The SAM results were generally inferior to those produced using the SVM method. While SAM was able to distinguish the larger nodules from the background sediment category, they were not always classified well, and many non-sediment pixels remained unclassified (Fig. 4c, g). Also, small megafauna and green spots were often not classified correctly. For example, in the lower left of Fig. 4g, SAM classified pixels as green spots whereas SVM classified these pixels as nodule or sediment (Fig. 4f), which appears to be supported by the pseudo-reflectance data (Fig. 4e). Larger megafauna such as the coral in Fig. 4g were generally classified well by SAM.

Due to the differences between the SVM and SAM classifications, the areal coverage estimations also varied by category. For the four tracks classified by SAM, the mean coverages for the nodule category (0.5–1.6%) and the shadow category (0.3–0.7%) were lower estimations than those determined by the SVM results (Fig. 5a). In contrast, coverage for the combined 16 fauna categories and the green spot category was estimated to be higher via the SAM method than the SVM method. Roughly 1% of the image pixels remained unclassified by SAM (Fig. 5a).

4.2.3. Accuracy of SAM relative to SVM

Based on the pseudo-reflectance images (Fig. 4a, e), SVM yielded a good classification of the nodule and shadow areas, as well as of most megafauna such as the crustacean and isopod in Fig. 4b and the coral in Fig. 4f. SAM also distinguished these areas from the background

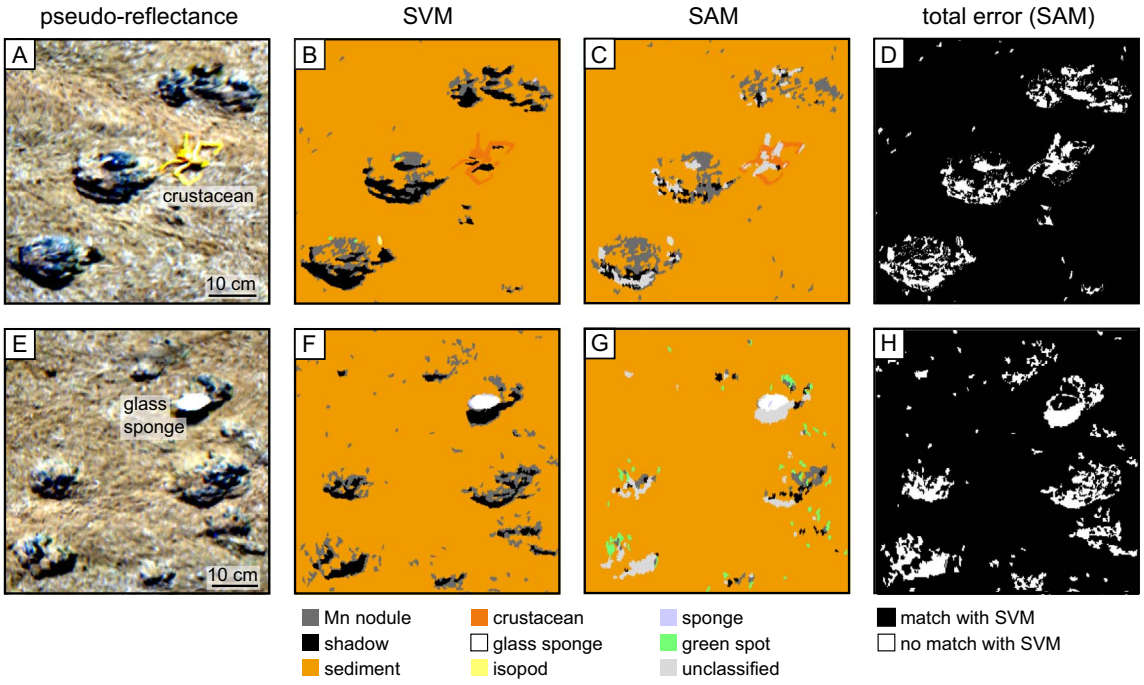

Fig. 4. Comparison of the SVM and SAM classification results for two examples (locations are shown in Fig. 1c). (a) and (e): pseudo-reflectance data (in pseudo-RGB with R: 645 nm, G: 571 nm, B: 473 nm), showing manganese nodules with a crustacean (Decapoda, Parapaguridae, *Probeebei mirabilis*) and an isopod (Isopoda, Munnopsidae) in (a) and manganese nodules with a glass sponge in (e). (b) and (f): SVM classification result after classification aggregation of 35 in (b) and 30 in (f). (c) and (g): SAM classification result after classification aggregation of 25 in (c) and 30 in (g). (d) and (h): total error of SAM relative to the SVM classification result.

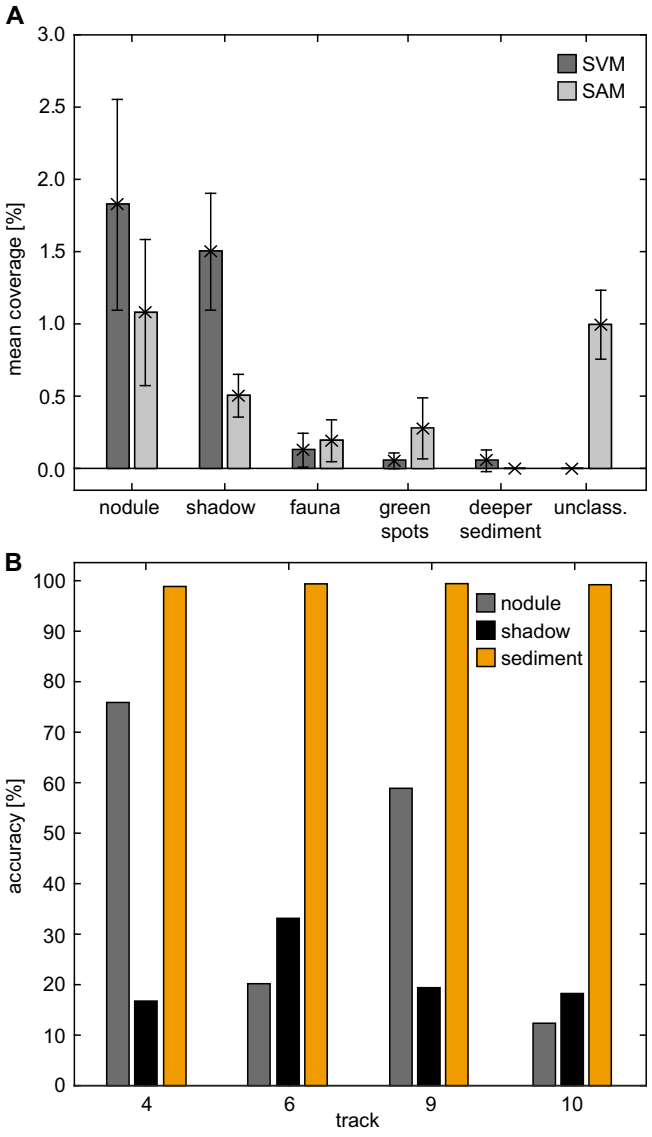

Fig. 5. (a) Mean coverage of each category for the SVM and SAM classifications, shown in percentage of the total number of pixels per track and excluding the background sediment category. The fauna category comprises 16 different megafauna detailed in Dumke et al. (in prep.). (b) Classification accuracy of SAM relative to SVM for the nodule, shadow, and background sediment categories on the four tracks classified by both methods (locations are shown in Fig. 1c). While the relative accuracy is high (> 98%) for the sediment category, it is much lower and more variable for the nodule and shadow categories.

sediment, and the coral, crustacean and parts of the nodule areas were classified in agreement with SVM (Fig. 4c, g). However, other non-sediment areas were assigned a different category, and many pixels, e.g. shadow pixels, were not classified at all.

The overall accuracy of SAM relative to SVM varied between 94.7% and 97.2%, as determined from direct comparison of the classification images via ENVI's confusion matrix tool. However, these high values were mostly due to the high accuracy for the background sediment category (98.8–99.4%; Fig. 5b), which constituted > 94% of the image pixels. For the other categories, the relative accuracy was much lower, with 12.3–75.9% for the nodule category and 16.7–33.1% for the shadow category (Fig. 5b). This discrepancy is further illustrated by the total error of the SAM classification as inferred from the confusion matrix (Fig. 4d, h). The pixels for which the SAM classification agreed with the SVM result mostly belonged to the background sediment category, whereas pixels of categories different from those assigned by SVM generally belonged to the non-sediment categories. Hence, while the SAM method was able to distinguish these non-sediment pixels from the background sediment, it was often not able to classify them in the same way as SVM.

4.3. Areal nodule density

On all tracks, case 1 resulted in less nodule objects being identified than the true number of nodules (Table 1). In contrast, the amount of nodules suggested by case 2 was overestimations of the numbers actually present on the seafloor. Therefore, using only the nodule category for the clumping method underestimated the number of nodules, while also taking into account the shadow category overestimated the amount.

Comparison with the UHI pseudo-RGB images showed that not all of the clumped objects were confirmed nodules. For case 1, on average 86.9% of the clumped objects were confirmed nodules, while for case 2, 76.0% of all objects represented nodules (Table 1). The remaining objects were false positive identifications, i.e., other anomalies not associated with nodules. For example, larger megafauna also caused shadows that were included in the case 2 objects.

In addition, some confirmed nodules were not included in the clumped objects and thus represented false negatives. Only 62.1% of the confirmed nodules corresponded to the clumped objects of case 1, whereas 86.5% were detected in case 2 (Table 1). Case 2 therefore included less false negatives but more false positives than case 1. Some tracks also exhibited double counts, i.e., two separate objects belonging to the same nodule, which further influenced the nodule count.

The different success rates of the nodule counts based on the two clumping methods are indicated in Fig. 6. The manual nodule count in the pseudo-reflectance data (Fig. 6a) and the video data revealed 17 nodules, which are generally also apparent in the SVM classification image (Fig. 6b). Case 1 detected 11 of these, with the remaining six representing false negatives (Fig. 6c, Table 1). In case 2 (Fig. 6d), the number of counted objects equals that of the manual count (17), but only 14 of these are confirmed nodules. The other three are two false positives and one double count where a nodule object and a shadow object belonging to the same nodule are not connected (Fig. 6d, Table 1). Three confirmed nodules were not detected by case 2 (false negatives). Note that in case 2, three nodules were detected that were not recognized by case 1.

Based on the number of confirmed nodules and the dimensions of the imaged areas, the reference nodule density varied between 6.9 and 11 nodules per m^2, with an average of 9.4 m^{-2}. The areal nodule density inferred from case 1 was generally lower (3.4–10.3 m^{-2}, average 7.0 m^{-2}); for case 2, it was higher (8.4–12.4 m^{-2}, average 10.7 m^{-2}). For the example in Fig. 6, the true areal nodule density is 8.4 m^{-2}, but the nodule count of case 1 resulted in a lower nodule density of 5.4 m^{-2}. Case 2 arrived at the correct density of 8.4 m^{-2}, though this is a result of the false positives numerically equalling the false negatives.

5. Discussion

In this study, we presented hyperspectral image data acquired in 4195 m water depth, using a UHI on an ROV. As it was the first time a hyperspectral imaging study of this kind was conducted in the deep sea, we first evaluate the acquisition setup used, before discussing the results of the supervised classifications as well as their implications.

5.1. Evaluation of the acquisition setup and suggestions for improvement

Acquisition of UHI data can be challenging, because several requirements have to be fulfilled by the underwater vehicle used as the mounting platform for the UHI. These requirements include the maintenance of constant velocity, heading and altitude, as well as high-resolution (about 5 kHz) navigation and vehicle attitude data (Johnsen

Table 1
Overview of the true number of nodules (manual count) and the nodule amount determined from the clumping results (clump count) for case 1 (nodule category only) and case 2 (nodule and shadow category). Track locations are shown in Fig. 1c.

Track	Manual count	Clump count	No. of correct nodules	Correct nodules: % of manual count	Correct nodules: % of growth count	Double count	False positive	False negative
Case 1								
4	32	12	12	37.50	100.00	0	0	20
5	38	38	30	78.95	78.95	0	8	8
6	25	24	18	72.00	75.00	1	5	7
7	17	11	11	64.71	100.00	0	0	6
8	36	34	29	80.56	85.29	0	5	7
9	34	17	17	50.00	100.00	0	0	17
10	28	27	21	75.00	77.78	0	6	7
12	58	38	32	55.17	84.21	5	1	26
14	29	16	13	81.25	81.25	2	1	16
Case 2								
4	32	43	26	81.25	60.47	4	13	6
5	38	43	33	86.84	76.74	1	9	5
6	25	32	22	88.00	68.75	0	10	3
7	17	17	14	82.35	82.35	1	2	3
8	36	42	32	88.89	76.19	0	10	4
9	34	47	34	100.00	72.34	0	13	0
10	28	31	25	89.29	80.65	0	6	3
12	58	50	38	65.52	76.00	3	9	20
14	29	31	28	96.55	90.32	0	3	1

et al., 2013, 2016; Tegdan et al., 2015). In addition, sufficiently even illumination is necessary. While the ROV used in this study met most of these requirements, the USBL navigation data was of too low accuracy, due to the great water depth, so the use of video-based navigation data (Nornes et al. (in prep.)) for geocorrection of the UHI data was a required additional processing step.

Issues with seafloor illumination were also encountered. As demonstrated by the radiance data (Fig. 2a), the acquisition setup was not optimal in terms of illumination. As a result, a prominent shadow caused by the manipulator arm holding the UHI was present in the data, which could not be avoided, as the UHI could not be mounted on the ROV in any more appropriate configuration. Smaller shadows occurring behind nodules and other elevated features were due to the positioning of the illumination source above and behind the UHI. If it had been possible to mount dedicated lamps on either side of the UHI, as has been done for shallow-water UHI surveys using ROVs (Johnsen et al., 2013, 2016; Tegdan et al., 2015), illumination would have been directly from above, which would have reduced the occurrence of shadows behind nodules. Moreover, the manipulator arm would not have influenced illumination. Fortunately, it was possible to remove the setup-induced shadow completely during post-processing, but we recommend that such a setup should be avoided in the future.

Due to the lack of dedicated lighting with a known spectrum, as well as lack of knowledge of the inherent optical properties of the water column, it was not possible to obtain an optimal illumination reference for reflectance processing. The applied reference spectra derived from the median-spectra approach resulted in generally good processing results, but they could not correct for all external influences and therefore resulted in pseudo-reflectance data rather than true reflectance data. Obtaining true reflectance data would have required more extensive processing, e.g. involving radiative transfer modelling to determine an accurate illumination reference for the light field of the combined ROV lamps, which was outside the scope of this study.

To provide a spectral classification of OOI, which was the aim of this study, true reflectance data were not necessarily required. However, for comparison of spectral signatures with spectra from existing spectral databases, as well as with spectral responses acquired in other areas or on different platforms, obtaining true reflectance data would be essential. Moreover, with true reflectance data a spectral database for endmember spectra could be set up. Such a database would facilitate supervised classification of potential future hyperspectral image data from the study area, as manual definition of ROIs to obtain endmember spectra would no longer be required if an OOI's reflectance spectrum is already contained in the database.

5.2. Relative accuracy of the classification methods

Our results show that the SVM method provided a more accurate classification than the SAM method. While the SVM results are interpreted as a good approximation of ground-truthing images, the SAM results contain unclassified pixels, and additionally, non-sediment pixels were often classified differently than by SVM. Visual comparison with the pseudo-reflectance data suggests that the SVM results appear generally correct, while the SAM results are likely erroneous when they differ from the SVM results. The discrepancies in estimations of seafloor coverage by the different categories between the two methods (Fig. 5a) are therefore thought to be largely due to misclassifications by the SAM method.

Although the SVM method is more accurate than SAM, it did not perform perfectly, as misclassification of pixels did occur. However, in the absence of suitable ground-truthing data, the true accuracy of the SVM method cannot be determined. Generally, visual comparison with the UHI pseudo-RGB images suggested that most of the exposed nodule surfaces, larger megafauna and shadows were classified accurately. However, very small patches classified as nodule or shadow often remained in between the larger features after classification aggregation (25–35 pixels) was applied. It is unclear whether these small pixels clusters were classified correctly. They could represent classification noise where the classification did not work well, but the UHI pseudo-RGB data are not conclusive in this regard, and potential features would be too small to be clearly resolved in the video data. Alternatively, at least the larger of these patches could represent small outcrops of nodules that have been almost completely buried, e.g. by re-sedimentation of the sediment plume produced by the 78 plough trawls comprising the DISCOL experiment. Another explanation could be small-scale terrain roughness causing shadows on the side facing away from the ROV lamps, but without micro-scale bathymetry, this can neither be confirmed nor excluded.

In the absence of ground-truthing images, absolute classification accuracies of the two classification methods used here could not be determined. Therefore, only estimates of relative accuracies were possible. Based on the very good classification results of the SVM method,

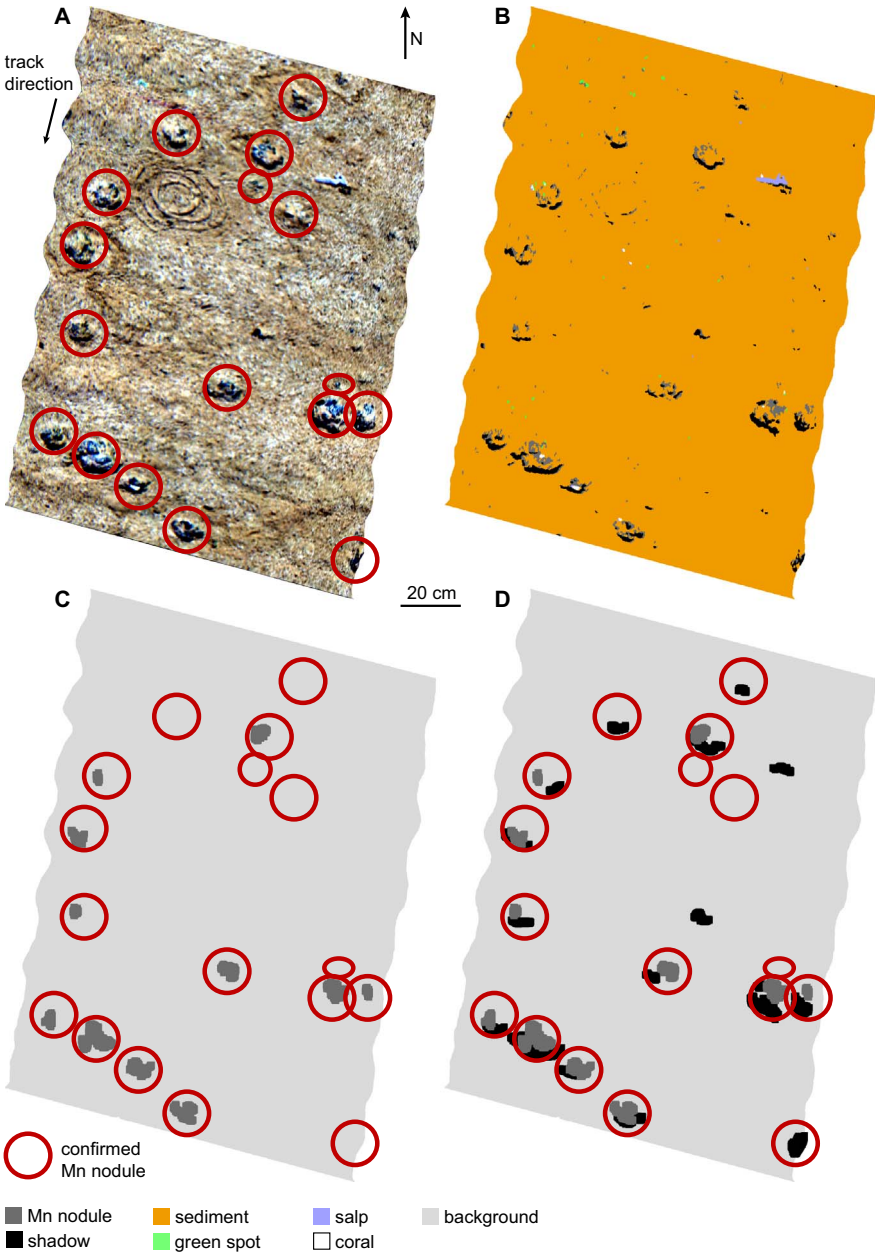

Fig. 6. (a) UHI pseudo-reflectance data (in pseudo-RGB) showing 17 manganese nodules highlighted by red circles, as well as a dead salp and a coral. (b) SVM classification image that served as a basis for the clumping of category areas. (c) Clump image for case 1 (nodule category only) based on the SVM classification image in (b). A total of 11 nodule objects were detected, with six false negatives marked by empty circles. (d) Clump image for case 2 (nodule category and shadow category combined) based on (b). Although 17 potential nodule objects were detected, they include two false positives and one double count, while three nodules were not detected (false negatives). (For interpretation of the references to colour in this figure legend, the reader is referred to the web version of this article.)

we estimate a classification accuracy of > 90% for the non-sediment categories and about 99% for the background sediment category. For SAM, the classification accuracy was considerably lower than for SVM and was estimated to about 40% for the non-sediment categories and > 90% for the background sediment category.

5.3. Detection of seafloor manganese nodules

Supervised classification using the SVM method is able to detect manganese nodules imaged in UHI data. This is shown by the clumping results and comparison of the potential nodule objects with the true nodule presence. Although it should be noted that the shape and size of the clumped objects do not necessarily represent the true nodule dimensions, the clumped objects indicate where nodules are suggested to be present based on the classification results.

When only the nodule category was used in the clumping procedure (case 1), in most cases not all nodules present were detected, which resulted in false negatives. Nevertheless, this approach is preferred over case 2, which generally overestimated the amount of nodules by introducing more false positives. The number of false negatives in the case 1 results could potentially be reduced by decreasing the degree of classification aggregation before the clumping process, thus allowing nodules marked by only small pixel clusters to be taken into account. However, this would also increase the number of false positives, as more non-nodule areas (misclassifications) would also be included.

In addition to nodule detection, the classification images also allowed estimating nodule coverage, which was about 1–4% in the SVM classification images. However, this amount only represents the minimum nodule coverage, given that most nodules were partly covered by sediment. As a nodule half covered by sediment will only have half of its surface area classified as nodule, the resulting category coverage is lower than the true nodule coverage. Therefore, coverage estimates derived from the clumped objects (1–6% for case 1 and 4–9% for case 2) are probably more realistic, even though they also include false positives and false negatives. Nodule coverages of up to 9% are in agreement with nodule coverages determined in other areas such as in the Clarion-Clipperton Zone (2–20%; Le Bas and North, 2016) and the Central Indian Ocean Basin (2–15%; Sharma et al., 2010).

Current methods for determining nodule coverage are largely based on conventional RGB photo imagery from which nodule coverage is derived through unsupervised or supervised classification (Sharma et al., 2010; Schoening et al., 2012, 2014), image segmentation methods (Schoening et al., 2016; Kuhn and Rathke, 2017), object-based image analysis (Le Bas and North, 2016), or kriging methods (Kuhn et al., 2016). High-resolution photo imagery has also been correlated with acoustic backscatter data to extrapolate nodule coverage over larger areas based on backscatter values (Chakraborty and Kodagali, 2004; Le Bas and North, 2016). In addition, image data can be combined with results from box corer samples to determine resource estimates in $kg\,m^{-2}$ (Kuhn et al., 2016; Kuhn and Rathke, 2017).

Hyperspectral image data provide an alternative to the conventional RGB imagery used by these approaches. Although it was beyond the scope of this study to directly compare the hyperspectral classification results to classification of RGB imagery, it is expected that the higher spectral resolution of hyperspectral data yield more accurate classification results than RGB imagery (Johnsen et al., 2013). Comparisons between hyperspectral and multispectral classifications (e.g. Hochberg and Atkinson, 2003) showed that hyperspectral classifications were generally superior to those based on fewer spectral bands. Hyperspectral imaging may thus provide a better basis for determining seafloor nodule coverage.

5.4. Potential for hyperspectral mapping of seafloor mineral resources

Our results show that underwater hyperspectral image data can be used similarly to conventional hyperspectral data to detect and evaluate mineral resources of interest for mining purposes. The main differences between the conventional approach applied in terrestrial mineral exploration and our underwater approach are the spectral band range and the areal coverage.

Conventional hyperspectral imaging for mineral exploration usually does not focus on the visible range. Instead, the near-infrared and infrared parts of the solar spectrum are used in preference (Resmini et al., 1997; Bierwirth et al., 1999; Sabins, 1999; Kruse et al., 2003), as these contain characteristic absorption minima in mineral spectra (Clark et al., 1990). However, our data indicate that mineral deposits such as manganese nodules are well imaged and spectrally distinct in the visible range. Based on these observations, we suggest that the necessary omission of near-infrared and infrared wavelengths in underwater hyperspectral imaging does not affect the detection of seafloor mineral resources.

Due to the requirement to maintain a low altitude of 1–2 m, resulting in a swath width of 1–2 m, UHI surveys have a much lower areal coverage than conventional hyperspectral surveys. UHIs are therefore only suitable for mapping small areas of up to a few 1000 m^2. Coverage could be increased by increasing the altitude to up to 7 m (approximately 7 m swath width), provided the illumination sources are strong enough to ensure sufficient seafloor illumination (S. Ekehaug, pers. comm.). Alternatively, an AUV could be used as UHI platform, which would allow increased coverage due to higher survey altitudes of 6–9 m and the autonomous operation mode (Sture et al., 2017.). However, in both cases, the image resolution and hence feature detectability would suffer. For low-altitude (1–2 m) ROV-based studies, the spatial resolution is considerably higher and allows more detailed mapping of deposits, including mapping of individual manganese nodules, as shown in this study.

With the growing interest in commercial deep-sea mining, the need for high-resolution seafloor exploration is also increasing (Van Dover, 2011; Boschen et al., 2013, 2016; Collins et al., 2013). While a UHI would not be suitable to map an entire mining claim, UHI surveys could be used for detailed investigations of target sites that were identified in larger-scale seabed data, e.g. acquired by acoustic methods.

As with terrestrial hyperspectral image data, seafloor hyperspectral images also have the potential to allow different types of mineral deposits to be distinguished (Johnsen et al., 2013). In the case of manganese nodules, compositions can vary over larger spatial scales, e.g. nodules from the Peru Basin differ in composition from those in the Clarion-Clipperton Zone (Glasby, 2000). These variations are, however, unlikely to be directly reflected by the nodule surfaces imaged by UHI surveys, and our data show that in the study area, spectral variations within the nodule category are low (Fig. 3). The potential for spectrally distinguishing different types of deposits is expected to be higher for hydrothermal deposits in massive sulphide areas, which are also a current target for potential future resource exploitation (Glasby, 2002; Rona, 2003; Hoagland et al., 2010; Boschen et al., 2013). First results (Dumke and Ellefmo, 2017) indicate that differences in the surface material composition of such deposits are apparent in UHI data.

6. Conclusions

In this study, we presented the first hyperspectral image data from the deep seafloor. Manganese nodules and seabed fauna may be well imaged at high spectral and spatial resolutions. Comparison of two supervised classification methods showed that the SVM method is superior to the SAM method in classifying manganese nodules as well as fauna and sediment anomalies. Nodule coverages within the surveyed region of the nodule field investigated were inferred from the SVM classification images and varied between 1 and 9% of the seafloor. Most nodule surfaces are not fully exposed due to sediment partially covering the top surfaces of nodules, which resulted in these sections of nodules being classified as sediment rather than nodule.

Our results show that underwater hyperspectral imaging allows extending seafloor hyperspectral surveys from shallow coastal waters to the deep sea, and therefore represents a promising new method for high-resolution mapping and classification of seafloor composition in terms of mineral deposit quantification. Moreover, the approach has a high potential for habitat mapping and environmental monitoring, e.g. in terms of fauna characterisation and distribution (Tegdan et al., 2015; Johnsen et al., 2016; Dumke et al., in prep.), which are also of high importance for environmental management in future mining areas (International Seabed Authority, 2012; Boschen et al., 2013, 2016; Durden et al., 2016; Vanreusel et al., 2016). Provided a broader exploration technique is applied first to identify areas of interest for high-resolution surveys, the UHI may become a promising tool for high-resolution seafloor exploration and monitoring in potential deep-sea mining areas.

Acknowledgements

This study received funding by the Norwegian Research Council (grant no. 250228) under the framework of JPI Oceans “MiningImpact”. Additional funding was provided by the European Union's Seventh Framework Programme for research, technological development and demonstration under the Blue Mining project (grant no. 604500) and by the Norwegian Research Council through the NTNU AMOS Centre of Excellence (grant no. 223254). Funding for the JPIO SONNE expedition SO242/2 and associated research was made available by the German Federal Ministry of Education and Research (BMBF; grant no. 03F0707A-G). Particular thanks are directed to chief scientist Antje Boetius, GEOMAR's KIEL6000 ROV team, as well as Captain Oliver Meyer and the crew of RV SONNE for their excellent support. Lars Martin Sandvik Aas and Stefan Ekehaug (both Ecotone AS) are thanked for advice on data processing. We also thank the associate editor and two anonymous reviewers for their constructive comments, which helped to improve the manuscript. The UHI data of cruise SO242/2 are available at https://doi.pangaea.de/10.1594/PANGAEA.874408.

References

Adam, E., Mutanga, O., Rugege, D., 2010. Multispectral and hyperspectral remote sensing for identification and mapping of wetland vegetation: a review. Wetl. Ecol. Manag. 18, 281–296. http://dx.doi.org/10.1007/s11273-009-9169-z.

Bierwirth, P., Blewett, R., Huston, D., 1999. Finding new mineral prospects with HYMAP: early results from a hyperspectral remote-sensing case study in the west Pilbara. AGSO Res. Newsl. 31, 29–31.

Bioucas-Dias, J.M., Plaza, A., Camps-Valls, G., Scheunders, P., Nasrabadi, N.M., Chanussot, J., 2013. Hyperspectral remote sensing data analysis and future challenges. IEEE Geosci. Remote Sens. Mag. 1, 6–36. http://dx.doi.org/10.1109/MGRS.2013.2244672.

Boetius, A. (Ed.), 2015. RV SONNE Fahrtbericht/Cruise Report SO242-2, JPI Oceans Ecological Aspects of Deep-sea Mining, DISCOL Revisited, Guayaquil-Guayaquil (Ecuador), 28.08.-01.10.2015. GEOMAR Report No. 27. GEOMAR Helmholtz Centre for Ocean Research, Kiel, Germany (552 pp.).

Borowski, C., 2001. Physically disturbed deep-sea macrofauna in the Peru Basin, southeast Pacific, revisited 7 years after the experimental impact. Deep-Sea Res. II 48, 3809–3839. http://dx.doi.org/10.1016/S0967-0645(01)00069-8.

Borowski, C., Thiel, H., 1998. Deep-sea macrofaunal impacts of a large-scale physical disturbance experiment in the Southeast Pacific. Deep-Sea Res. II 45, 55–81.

Boschen, R.E., Rowden, A.A., Clark, M.R., Gardner, J.P.A., 2013. Mining of deep-sea seafloor massive sulfides: a review of the deposits, their benthic communities, impacts from mining, regulatory frameworks and management strategies. Ocean Coast. Manag. 84, 54–67. http://dx.doi.org/10.1016/j.ocecoaman.2013.07.005.

Boschen, R.E., Rowden, A.A., Clark, M.R., Pallentin, A., Gardner, J.P.A., 2016. Seafloor massive sulfide deposits support unique megafaunal assemblages: implications for seabed mining and conservation. Mar. Environ. Res. 115, 78–88. http://dx.doi.org/10.1016/j.marenvres.2016.02.005.

Camps-Valls, G., Gómez-Chova, L., Calpe-Maravilla, J., Martín-Guerrero, J.D., Soria-Olivas, E., Alonso-Chordá, L., Moreno, J., 2004. Robust support vector method for hyperspectral data classification and knowledge discovery. IEEE Trans. Geosci. Remote Sens. 42, 1530–1542. http://dx.doi.org/10.1109/TGRS.2004.827262.

Chakraborty, B., Kodagali, V., 2004. Characterizing Indian Ocean manganese nodule-bearing seafloor using multi-beam angular backscatter. Geo-Mar. Lett. 24, 8–13. http://dx.doi.org/10.1007/s00367-003-0153-y.

Chang, G., Mahoney, K., Briggs-Whitmire, A., Kohler, D.D.R., Mobley, C.D., Lewis, M., Moline, M.A., Boss, E., Kim, M., Philpot, W., Dickey, T.D., 2004. The new age of hyperspectral oceanography. Oceanography 17, 16–23. http://dx.doi.org/10.5670/oceanog.2004.43.

Chennu, A., Färber, P., Volkenborn, N., Al-Najjar, M.A.A., Janssen, F., de Beer, D., Polerecky, L., 2013. Hyperspectral imaging of the microscale distribution and dynamics of microphytobenthos in intertidal sediments. Limnol. Oceanogr. Methods 11, 511–528. http://dx.doi.org/10.4319/lom.2013.11.511.

Clark, R.N., King, T.V.V., Klejwa, M., Swayze, G.A., 1990. High spectral resolution reflectance spectroscopy of minerals. J. Geophys. Res. 95, 12653–12680. http://dx.doi.org/10.1029/JB095iB08p12653.

Collins, P.C., Croot, P., Carlsson, J., Colaço, A., Grehan, A., Hyeong, K., Kennedy, R., Mohn, C., Smith, S., Yamamoto, H., Rowden, A., 2013. A primer for the environmental impact assessment of mining at seafloor massive sulfide deposits. Mar. Policy 42, 198–209. http://dx.doi.org/10.1016/j.marpol.2013.01.020.

Cronan, D.S., Tooms, J.S., 1969. The geochemistry of manganese nodules and associated pelagic deposits from the Pacific and Indian Oceans. Deep-Sea Res. 16, 335–359. http://dx.doi.org/10.1016/0011-7471(69)90003-5.

Daase, M. (Ed.), 2016. Cruise Report – Polar Night Cruise 2016. University of Tromsø (39 pp.).

Dell'Acqua, F., Gamba, P., Ferrari, A., Palmason, J.A., Benediktsson, J.A., Arnason, K., 2004. Exploiting spectral and spatial information in hyperspectral urban data with high resolution. IEEE Geosci. Remote Sens. Lett. 1, 322–326. http://dx.doi.org/10.1109/LGRS.2004.837009.

Dickey, T., Lewis, M., Chang, G., 2006. Optical oceanography: recent advances and future directions using global remote sensing and in situ observations. Rev. Geophys. 44, RG1001. http://dx.doi.org/10.1029/2003RG000148.

Dierssen, H.M., 2013. Overview of hyperspectral remote sensing for mapping marine benthic habitats from airborne and underwater sensors. Imaging Spectrometry XVIII. Proc. SPIE 1–7. http://dx.doi.org/10.1117/12.2026529.

Dierssen, H.M., Randolph, K., 2013. Remote sensing of ocean color. In: Encyclopedia of Sustainability Science and Technology. Springer. http://dx.doi.org/10.1007/978-1-4614-5684-1_18.

Dierssen, H.M., Chlus, A., Russell, B., 2015. Hyperspectral discrimination of floating mats of seagrass wrack and the macroalgae *Sargassum* in coastal waters of Greater Florida Bay using airborne remote sensing. Remote Sens. Environ. 167, 247–258. http://dx.doi.org/10.1016/j.rse.2015.01.027.

Dumke, I., Ellefmo, S.L., 2017. Report on visual data acquisition in the field and interpretation for SMS. In: Blue Mining Deliverable D1.31, Blue Mining Project, European Commission Seventh Framework Programme, (33 pp.).

Dumke, I., Purser, A., Marcon, Y., Nornes, S.M., Johnsen, G., Ludvigsen, M., Søreide, F., 2018. Underwater hyperspectral imaging as an in-situ taxonomic tool for deep-sea megafauna (unpublished). .

Durden, J.M., Billett, D.S.M., Brown, A., Dale, A.C., Goulding, L., Gollner, S., Murphy, K., Pape, E., Purser, A., Rolin, J.-F., Smith, A.J., Stewart, I., Turner, P.J., de Wachter, T., Weaver, P.P.E., van Dover, C.L., Verlaan, P., Jones, D.O.B., 2016. Report on the Managing Impacts of Deep-seA reSource exploitation (MIDAS) workshop on environmental management of deep-sea mining. Res. Ideas Outcomes 2, e10292. http://dx.doi.org/10.3897/rio.2.e10292.

Fearns, P.R.C., Klonowski, W., Babcock, R.C., England, P., Phillips, J., 2011. Shallow water substrate mapping using hyperspectral remote sensing. Cont. Shelf Res. 31, 1249–1259. http://dx.doi.org/10.1016/j.csr.2011.04.005.

Foell, E.J., Thiel, H., Schriever, G., 1990. DISCOL: A Long-term, Large-scale, Disturbance-recolonization Experiment in the Abyssal Eastern Tropical South Pacific Ocean. Offshore Technology Conference 1990, Houston, Texas. pp. 497–503. http://dx.doi.org/10.4043/6328-MS.

Fossen, T.I., 2011. Handbook of Marine Craft Hydrodynamics and Motion Control. John Wiley and Sons, UK.

Glasby, G.P., 1972. The mineralogy of manganese nodules from a range of marine environments. Mar. Geol. 13, 57–72. http://dx.doi.org/10.1016/0025-3227(72)90071-0.

Glasby, G.P., 2000. Manganese: predominant role of nodules and crusts. In: Schulz, H.D., Zable, M. (Eds.), Marine Geochemistry. Springer, Berlin, pp. 335–372.

Glasby, G.P., 2002. Deep seabed mining: past failures and future prospects. Mar. Georesour. Geotechnol. 20, 161–176. http://dx.doi.org/10.1080/03608860290051859.

Goetz, A.F.H., 2009. Three decades of hyperspectral remote sensing of the Earth: a personal view. Remote Sens. Environ. 113, S5–S16. http://dx.doi.org/10.1016/j.rse.2007.12.014.

Goetz, A.F.H., Vane, G., Solomon, J.E., Rock, B.N., 1985. Imaging spectrometry for Earth remote sensing. Science 228, 1147–1153. http://dx.doi.org/10.1126/science.228.4704.1147.

Greinert, J. (Ed.), 2015. RV SONNE Fahrtbericht/Cruise Report SO242-1, JPI Oceans Ecological Aspects of Deep-Sea Mining, DISCOL Revisited, Guayaquil-Guayaquil (Ecuador), 28.07.-25.08.2015. GEOMAR Report No. 26. GEOMAR Helmholtz Centre for Ocean Research, Kiel, Germany (290 pp.).

Gwyther, D., 2008. Environmental Impact Statement, Solwara 1 Project. Nautilus Minerals Niugini Limited, Main Report. Coffey Natural Systems, Brisbane.

Hakvoort, H., Heymann, K., Stein, C., Murphy, D., 1997. In-situ optical measurements of sediment type and phytobenthos of tidal flats: a basis for imaging remote sensing spectroscopy. In: Deutsche Hydrographische Zeitschrift. 49http://dx.doi.org/10.1007/BF02764045. (367-272).

Herold, M., Roberts, D., Smadi, O., Noronha, V., 2004. Road Condition Mapping Using Hyperspectral Remote Sensing. 2004 AVIRIS Workshop, Pasadena, California. (15 pp.).

Hoagland, P., Beaulieu, S., Tivey, M.A., Eggert, R.G., German, C., Glowka, L., Lin, J., 2010. Deep-sea mining of seafloor massive sulfides. Mar. Policy 34, 728–732. http://dx.doi.org/10.1016/j.marpol.2009.12.001.

Hochberg, E.J., Atkinson, M.J., 2000. Spectral discrimination of coral reef benthic communities. Coral Reefs 19, 164–171. http://dx.doi.org/10.1007/s003380000087.

Hochberg, E.J., Atkinson, M.J., 2003. Capabilities of remote sensors to classify coral, algae, and sand as pure and mixed spectra. Remote Sens. Environ. 85, 174–189. http://dx.doi.org/10.1016/S0034-4257(02)00202-X.

International Seabed Authority, 2012. Environmental management needs for exploration and exploitation of deep sea minerals. ISA Technical Study Series 10. International Seabed Authority, Kingston, Jamaica.

Johnsen, G., Volent, Z., Dierssen, H., Pettersen, R., Van Ardelan, M., Søreide, F., Fearns, P., Ludvigsen, M., Moline, M., 2013. Underwater hyperspectral imagery to create biogeochemical maps of seafloor properties. In: Watson, J., Zielinski, O. (Eds.), Subsea Optics and Imaging. Woodhead Publishing Ltd., Cambridge, pp. 508–535.

Johnsen, G., Ludvigsen, M., Sørensen, A., Sandvik Aas, L.M., 2016. The use of underwater hyperspectral imaging deployed on remotely operated vehicles – methods and applications. IFAC-PapersOnLine 49 (23), 476–481. http://dx.doi.org/10.1016/j.ifacol.2016.10.451.

Klonowski, W.M., Fearns, P.R.C.S., Lynch, M.J., 2007. Retrieving key benthic cover types and bathymetry from hyperspectral imagery. J. Appl. Remote Sens. 1, 011505. http://dx.doi.org/10.1117/1.2816113.

Kruse, F.A., Lefkoff, A.B., Boardman, J.W., Heidebrecht, K.B., Shapiro, A.T., Barloon, P.J., Goetz, A.F.H., 1993. The Spectral Image Processing System (SIPS) – interactive visualization and analysis of imaging spectrometer data. Remote Sens. Environ. 44, 145–163. http://dx.doi.org/10.1016/0034-4257(93)90013-N.

Kruse, F.A., Boardman, J.W., Huntington, J.F., 2003. Comparison of airborne hyperspectral data and EO-1 Hyperion for mineral mapping. IEEE Trans. Geosci. Remote Sens. 41, 1388–1400. http://dx.doi.org/10.1109/TGRS.2003.812908.

Kuhn, T., Rathke, M., 2017. Report on Visual Data Acquisition in the Field and Interpretation for SMnN. Blue Mining Deliverable D1.31, Blue Mining project, European Commission Seventh Framework Programme. (34 pp.).

Kuhn, T., Rühlemann, C., Knobloch, A., 2016. Classification of manganese nodule estimates: can we reach the “measured resource” level? In: Hong, S., Morgen, C.L. (Eds.), Resource and Environmental Assessments for Seafloor Mining Development. Underwater Mining Conference 2016, Incheon, Korea, (6 pp.).

Kutser, T., Miller, I., Jupp, D.L.B., 2006. Mapping coral reef benthic substrates using hyperspectral space-borne images and spectral libraries. Estuar. Coast. Shelf Sci. 70, 449–460. http://dx.doi.org/10.1016/j.ecss.2006.06.026.

Landmann, T., Piiroinen, R., Makori, D.M., Abdel-Rahman, E.M., Makau, S., Pellikka, P., Raina, S.K., 2015. Application of hyperspectral remote sensing for flower mapping in African savannas. Remote Sens. Environ. 166, 50–60. http://dx.doi.org/10.1016/j.rse.2015.06.006.

Le Bas, T., North, L., 2016. Acoustic Model for Seafloor FeMn Nodules. Blue Mining Deliverable D2.51, Blue Mining Project, European Commission Seventh Framework Programme. (62 pp.).

Ludvigsen, M., Aasly, K., Ellefmo, S., Hilario, A., Ramirez-Llodra, E., Søreide, F., Falcon-Suarez, I., Juliani, C., Kieswetter, A., Lim, A., Malmquist, C., Nornes, S.M., Paulsen, E., Reimers, H., Sture, Ø., 2016. MarMine Cruise Report. NTNU Cruise Reports 2016 No. 1. (108 pp.).

Mazel, C.H., 1997. Diver-operated instrument for in situ measurement of spectral fluorescence and reflectance of benthic marine organisms and substrates. Opt. Eng. 36. http://dx.doi.org/10.1117/1.601486.

Melgani, F., Bruzzone, L., 2004. Classification of hyperspectral remote sensing images with support vector machines. IEEE Trans. Geosci. Remote Sens. 42, 1778–1790. http://dx.doi.org/10.1109/TGRS.2004.831865.

Mountrakis, G., Im, J., Ogole, C., 2011. Support vector machines in remote sensing: a review. ISPRS J. Photogramm. Remote Sens. 66, 247–259. http://dx.doi.org/10.1016/j.isprsjprs.2010.11.001.

Nornes, S.M., Ødegård, Ø., Dumke, I., Ludvigsen, M., Johnsen, G., Sørensen, A.J., 2018. Unmanned underwater vehicle-based photogrammetry for marine benthic mapping. (unpublished).

Petit, T., Bajjouk, T., Mouquet, P., Rochette, S., Vozel, B., Delacourt, C., 2017. Hyperspectral remote sensing of coral reefs by semi-analytical model inversion – comparison of different inversion setups. Remote Sens. Environ. 190, 348–365. http://dx.doi.org/10.1016/j.rse.2017.01.004.

Pettersen, R., Johnsen, G., Bruheim, P., Andreassen, T., 2014. Development of hyperspectral imaging as a bio-optical taxonomic tool for pigmented marine organisms. Org. Divers. Evol. 14, 237–246. http://dx.doi.org/10.1007/s13127-013-0163-1.

Pons, S., Aymerich, I.F., Torrecilla, E., Piera, J., 2007. Monolithic spectrometer for environmental monitoring applications. In: Proceedings of IEEE/OEE Oceans Conference and Exhibition, OCEANS'07 Europe, Aberdeen, http://dx.doi.org/10.1109/OCEANSE.2007.4302402. (3 pp.).

Ramírez-Pérez, M., Röttgers, R., Torrecilla, E., Piera, J., 2015. Cost-effective hyperspectral transmissometers for oceanographic applications: performance analysis. Sensors 15, 20967–20989. http://dx.doi.org/10.3390/s150920967.

Reddy, A., 2010. Image processing and counting using MATLAB. http://www.instructables.com/id/Image-Processing-and-Counting-using-MATLAB/, Accessed date: 19 April 2017.

Resmini, R.G., Kappus, M.E., Aldrich, W.S., Harsanyi, J.C., Anderson, M., 1997. Mineral mapping with Hyperspectral Digital Imagery Collection Experiment (HYDICE) sensor data at Cuprite, Nevada, U.S.A. Int. J. Remote Sens. 18, 1553–1570. http://dx.doi.org/10.1080/014311697218278.

Roessner, S., Segl, K., Heiden, U., Kaufmann, H., 2001. Automated differentiation of urban surfaces based on airborne hyperspectral imagery. IEEE Trans. Geosci. Remote Sens. 39, 1525–1532. http://dx.doi.org/10.1109/36.934082.

Rona, P.A., 2003. Resources of the sea floor. Science 299, 673–674. http://dx.doi.org/10.1126/science.1080679.

Sabins, F.F., 1999. Remote sensing for mineral exploration. Ore Geol. Rev. 14, 157–183. http://dx.doi.org/10.1016/S0169-1368(99)00007-4.

Schoening, T., Kuhn, T., Nattkemper, T.W., 2012. Estimation of poly-metallic nodule coverage in benthic images. In: Proceedings of the 41st Conference of the Underwater Mining Institute. UMI.

Schoening, T., Kuhn, T., Nattkemper, T.W., 2014. Seabed classification using a bag-of-prototypes feature representation. In: 2014 ICPR Workshop on Computer Vision for Analysis of Underwater Imagery (CVAUI). IEEE, pp. 17–24. http://dx.doi.org/10.1109/CVAUI.2014.9.

Schoening, T., Kuhn, T., Jones, D.O.B., Simon-Lledo, E., Nattkemper, T.W., 2016. Fully automated image segmentation for benthic resource assessment of poly-metallic nodules. Methods Oceanogr. 15–16, 78–89. http://dx.doi.org/10.1016/j.mio.2016.04.002.

Schriever, G., 1995. DISCOL – disturbance and recolonization experiment of a manganese nodule area of the Southeastern Pacific. In: Proceedings of the ISOPE – Ocean Mining Symposium 1995, Tsukuba, Japan, pp. 163–166.

Sharma, R., Sankar, S.J., Samanta, S., Sardar, A.A., Gracious, D., 2010. Image analysis of seafloor photographs for estimation of deep-sea minerals. Geo-Mar. Lett. 30, 617–626. http://dx.doi.org/10.1007/s00367-010-0205-z.

Sohn, Y., Rebello, N.S., 2002. Supervised and unsupervised spectral angle classifiers. Photogramm. Eng. Remote Sens. 68, 1271–1280.

Sture, Ø., Ludvigsen, M., Søreide, F., Sandvik Aas, L.M., 2017. Autonomous Underwater Vehicles as a Platform for Underwater Hyperspectral Imaging. OCEANS 2017 MTS/IEEE, Aberdeen, UK. http://dx.doi.org/10.1109/OCEANSE.2017.8084995.

Tegdan, J., Ekehaug, S., Myrnes Hansen, I., Sandvik Aas, L.M., Steen, K.J., Pettersen, R., Beuchel, F., Camus, L., 2015. Underwater hyperspectral imaging for environmental mapping and monitoring of seabed habitats. OCEANS 2015, Genova. http://dx.doi.org/10.1109/OCEANS-Genova.2015.7271703. (6 pp.).

Thiel, H., Schriever, G., 1989. Cruise Report DISCOL 1, SONNE – Cruise 61. Berichte aus dem Zentrum für Meeres- und Klimaforschung der Universität Hamburg. 3 (75 pp.).

Underwood, E., Ustin, S., DiPietro, D., 2003. Mapping nonnative plants using hyperspectral imagery. Remote Sens. Environ. 86, 150–161. http://dx.doi.org/10.1016/S0034-4257(03)00096-8.

van der Meer, F.D., van der Werff, H.M.A., van Ruitenbeek, F.J.A., Hecker, C.A., Bakker, W.H., Noomen, M.F., van der Meijde, M., Carranza, E.J.M., de Smeth, J.B., Woldai, T., 2012. Multi- and hyperspectral geologic remote sensing: a review. Int. J. Appl. Earth Obs. Geoinf. 14, 112–128. http://dx.doi.org/10.1016/j.jag.2011.08.002.

Van Dover, C.L., 2011. Mining seafloor massive sulphides and biodiversity: what is at risk? ICES J. Mar. Sci. 68, 341–348. http://dx.doi.org/10.1093/icesjms/fsq086.

Vanreusel, A., Hilario, A., Ribeiro, P., Menot, L., Martínez Arbizu, P., 2016. Threatened by mining, polymetallic nodules are required to preserve abyssal epifauna. Sci. Rep. 6 (26808). http://dx.doi.org/10.1038/srep26808.

Volent, Z., Johnsen, G., Sigernes, F., 2007. Kelp forest mapping by use of airborne hyperspectral imager. J. Appl. Remote Sens. 1, 011503. http://dx.doi.org/10.1117/1.2822611.